

Imaging strain localization by X-ray radiography and digital image correlation: Deformation bands in Rothbach sandstone

Laurent Louis ^{a,*}, Teng-Fong Wong ^a, Patrick Baud ^b

^a Department of Geosciences, State University of New York at Stony Brook, Stony Brook, NY 11794-2100, USA

^b Institut de Physique du Globe (CNRS/ULP), 5 rue Descartes, 67084 Strasbourg, France

Received 15 December 2005; received in revised form 16 July 2006; accepted 21 July 2006

Available online 18 September 2006

Abstract

Three samples of Rothbach sandstone cored perpendicular, obliquely (45°) and parallel to the bedding were triaxially compacted at 140 MPa effective pressure. X-ray radiographs were acquired before and after the experiment, and two-dimensional digital image correlation (DIC) was used to map out the spatial distribution of compactive strain in these samples and investigate the effect of the bedding on the development of strain localization. Our technique could resolve the spatial distribution of strains on the order of 10⁻³, and DIC of X-ray radiographs of the three samples underscores different modes of localization. While diffuse compaction bands and compactive shear bands developed in the samples perpendicular and oblique to bedding, relatively homogenous compaction was observed in the sample cored parallel to bedding. The strain patterns inferred from 2D DIC were confirmed by complementary microstructural study including quantitative characterization of crack density. This feasibility study demonstrates the potential of extending this technique to higher resolutions using 3D X-ray CT data of triaxially compressed rock samples.

© 2006 Elsevier Ltd. All rights reserved.

Keywords: Compaction localization; Sandstone; Microscopy; X-ray radiography; Digital image correlation

1. Introduction

Strain localization occurs over a broad range of length scales, from centimeter-sized laboratory samples all the way up to crustal fault zones extending over hundreds of kilometers. While laboratory studies under controlled conditions of stress and pore pressure have already provided useful insights into the mechanics of strain localization (Paterson and Wong, 2005), before one extrapolates to natural settings it is essential to also have complementary observations on the deformation mechanisms and geometric complexity associated with the development of strain localization.

X-ray imaging is a powerful nondestructive technique for characterizing density distribution in geomaterials. When acquired on the same object along various angles, the resulting series of images (or views) can be used to reconstruct a 3D volume of the sample studied. Such a technique, known as X-ray computed tomography (CT), has recently been used in many geologic applications (Lindquist et al., 2000; Arns et al., 2001, 2002; Renard et al., 2004; Fredrich et al., 2006). The void space in porous rock significantly perturbs the attenuation within a volume element, and accordingly CT data can be used to infer the spatial distribution of porosity (Wellington and Vinegar, 1987; Ketcham and Iturrino, 2005). Depending on the resolution, a voxel may be totally or partially embedded within a pore or even comprise several pores. Many studies have been conducted using conventional medical CT, which typically has a spatial resolution on the order of 1 mm. These studies (e.g. Raynaud et al., 1989; Kawakata et al., 1999; Bésuelle et al., 2003) have focused on characterizing the damage evolution related to shear localization during

* Corresponding author now at: Département des Sciences de la Terre et de l'Environnement, UMR CNRS 7072, Université de Cergy–Pontoise, Bâtiment Neuville 3.1, 5, mail Gay–Lussac, Neuville–sur–Oise, F–95031 Cergy–Pontoise, France.

E-mail address: laurent.louis@geol.u-cergy.fr (L. Louis).

dilatant failure. In contrast, relatively little research has been performed using either “industrial” CT (with resolution ~ 0.1 mm) or microtomography to map out damage distribution in deformed and failed rock samples (Viggiani et al., 2004; Lenoir, 2006).

In a recent study (Louis et al., 2005), X-ray CT-measurement with sub-millimeter resolution was employed to image compactant cataclastic structures and investigate the development of discrete compaction bands in Diemelstadt sandstone. To map out the strain localization features, a statistical technique was developed which hinges on the observation that inelastic compaction in a porous sandstone (primarily involving grain crushing and pore collapse) would homogenize the spatial distribution of X-ray attenuation, and accordingly the local damage intensity can be inferred from the dispersion coefficient (standard deviation normalized by the mean) of the CT-values in an elemental volume made up of multiple voxels. By mapping out localized zones with relatively low dispersion coefficients as proxies for compaction bands, the geometric attributes such as the thickness and tortuosity of compaction bands in Diemelstadt sandstone were quantified and demonstrated to be in good agreement with microstructural observations.

However, Louis et al. (2005) also emphasized that such a dispersion analysis is useful for mapping out localized compaction in a deformed sample only if the rock initially does not have strong heterogeneities such as bedding foliation. Using Rothbach sandstone as an example they showed that thin lamination of relatively high density pervasive in this rock is manifested by appreciable reduction of dispersion coefficient, which would significantly complicate the identification of compaction bands also associated with lower dispersion coefficients. Hence, a fundamentally different approach needs to be formulated to characterize strain localization in such a rock with initial heterogeneities.

Digital image correlation is a technique that has been widely used in experimental mechanics to map out the spatial distribution of strain measured by moiré fringe, speckle interferometry, and recently X-ray CT (Chu et al., 1985; Bruck et al., 1989; Bay et al., 1999; Wang and Cuitiño, 2002). Since it hinges on the correlation between the digital image of an undeformed sample and that acquired after the same sample had undergone deformation, the technique can only be employed in conjunction with a nondestructive imaging system. An important advantage of this technique is that it can be applied to materials which are strongly anisotropic and heterogeneous. To our knowledge, limited DIC studies have been conducted on geomaterials in conjunction with X-ray imaging (Bhandari and Inoue, 2005; Lenoir, 2006) and none characterizing compactive strain localization. The first objective of this study was to evaluate the relevance of this technique to mapping out compaction localization in Rothbach sandstone using X-ray imaging. Our data set consists of X-ray radiographs (planar projection of the whole specimen attenuation characteristics) of the undeformed and deformed samples. Since a single image was used at each stage of deformation, it may be considered as a zeroth order tomography. This is meant to be used as

a feasibility study of future investigations on localized compaction with multi-sliced X-ray CT data. The other objective was to characterize the effect of bedding foliation on the failure mode in sandstone. Rothbach sandstone samples cored in three different orientations relative to the bedding were investigated. The failure modes imaged by X-ray radiography and two-dimensional DIC were compared with microstructural observations on petrographic thin sections.

2. Sample preparation and X-ray radiography

Rothbach sandstone has a nominal porosity of 20.0% and average grain radius of 110 μm . Its modal composition is 68% quartz, 16% feldspar, 3% oxides and micas and about 6% clays. Our samples were cored from the block studied by Baud et al. (2004). The sample RotQ3 was cored along an axis at 45° to the bedding, and the samples RotH4 and RotP3 were cored parallel and perpendicular to the bedding, respectively. All samples were cylindrical, with diameter of 18.4 mm and length 38.1 mm. After they had been cored these samples were sent to the High-Resolution CT Facility at the University of Texas at Austin for imaging, and subsequently these samples were used for mechanical deformation experiments.

The mechanical tests were conducted following the methodology of Wong et al. (1997). The jacketed samples were saturated with distilled water and deformed in the conventional triaxial configuration at room temperature under drained conditions at fixed pore pressure of 10 MPa and nominal axial strain rate of $1.3 \times 10^{-5} \text{ s}^{-1}$. Acoustic emission (AE) activity was monitored during these experiments. After the deformed samples were unloaded and retrieved from the pressure vessel, the jackets were carefully removed and the samples were exposed to the atmosphere for several weeks. The nominally dry samples were then sent to Austin for a second round of imaging.

The High-Resolution CT Facility there employs a 200 kV microfocal X-ray source capable of a $<10 \mu\text{m}$ focal spot size, and our data were typically acquired with the source at a peak energy of 180 kV. The methodology for data acquisition and analysis was as described by Ketcham and Carlson (2001). In this pilot study, we concentrated on correlation of 2D radiographs which can be conveniently compared with microstructural observations on thin sections. As described in Fig. 1, radiographs with pixel size 21.24 μm were obtained by lighting the specimen with a planar X-ray beam at regular intervals along its symmetry axis. The plane of the radiograph was chosen so that it is parallel to the plane formed by the specimen symmetry axis and the dip line of the bedding. Given the strong bedding in the Rothbach sandstone, the pre-existing heterogeneity in local porosity or effective density along the x -direction (Fig. 1) is expected to be small relative to that in the y - or z -directions. If the bedding also exerts strong influence on the failure mode and development of strain localization, then it is plausible that the spatial variation of strain concentrates on the (y, z) plane in the failed samples.

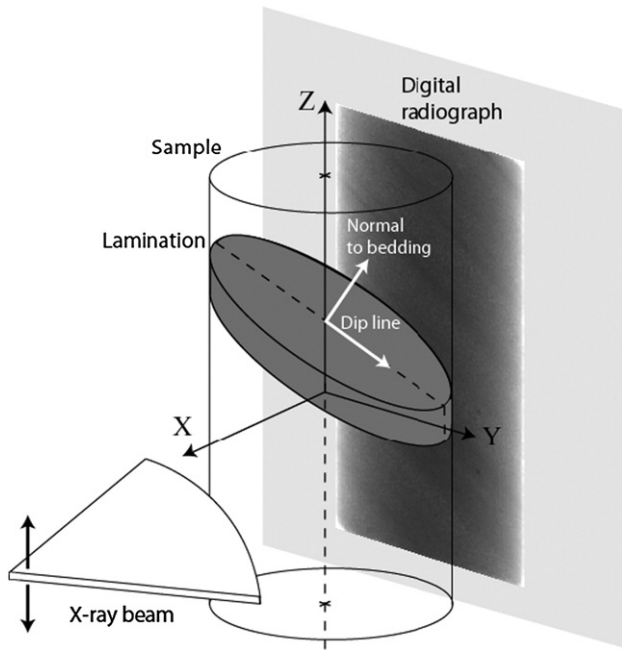


Fig. 1. Acquisition of X-ray radiographs and choice of the projection plane for a sample with strong bedding lamination inclined at an angle to the axial direction. Radiographs are typically acquired using a 2D fan beam across which the specimen is translated to image successive levels. Here the plane of the radiograph is perpendicular to the bedding strike (X) and the in-plane resolution (along Y and Z axes on the radiograph) is $21.24 \mu\text{m}$.

Since X-ray attenuation increases with increasing atomic number (if it is predominately due to photoelectric and Compton effects), the X-ray attenuation in a porosity-free material is dependent on the solid grain mineralogy, whereas in a porous rock the void space significantly lowers this attenuation and leads to partial volume effects (Ketcham, 2005) with attenuation values that are determined by the respective proportions of matrix and void space enclosed in the voxels. This particularity has been used to infer the spatial distribution of porosity and for some cases calibrations performed on porous rocks and soils

(Vinegar et al., 1991; Desrues et al., 1996) have established linear relationship between X-ray attenuation and local density.

3. Mechanical data and failure mode

In this paper we will use the convention with compressive stresses and compressive strains taken as positive. We will denote the maximum and minimum (compressive) principal stresses by σ_1 and σ_3 , respectively. The pore pressure will be denoted by P_p , and the difference $P_c - P_p$ between the confining pressure ($P_c = \sigma_2 = \sigma_3$) and pore pressure will be referred to as the “effective pressure” P_{eff} . The effective mean stress $(\sigma_1 + 2\sigma_3)/3 - P_p$ will be denoted by P and the differential stress $\sigma_1 - \sigma_3$ by Q .

Bésuelle et al. (2003) deformed 15 Rothbach sandstone samples (cored perpendicular to bedding) at effective pressures ranging from 5 MPa to 130 MPa. In Fig. 2 selected data from this previous study for the differential stress as a function of axial strain are shown, together with our data for samples RotP5 and RotP3 (imaged by radiography) both cored perpendicular to bedding at effective pressures of 10 MPa and 130 MPa, respectively. At effective pressure up to 20 MPa, the mechanical response and failure mode were typical of the brittle faulting regime. The differential stress attained a peak, beyond which strain softening was observed (Fig. 2a). At effective pressures of 40 MPa and higher, a sample would show shear-enhanced compaction (Wong et al., 1997) that initiated at the yield stress C^* , beyond which the data for effective mean stress as a function of porosity change (Fig. 2b) would show an accelerated decrease in volume in comparison to the hydrostat. A surge in AE activity was commonly observed beyond C^* . While visual examination of the samples that had undergone shear-enhanced compaction did not reveal features that would suggest strain localization, the X-ray data presented in this study could resolve localized structures that had actually developed in the interior of sample RotP3.

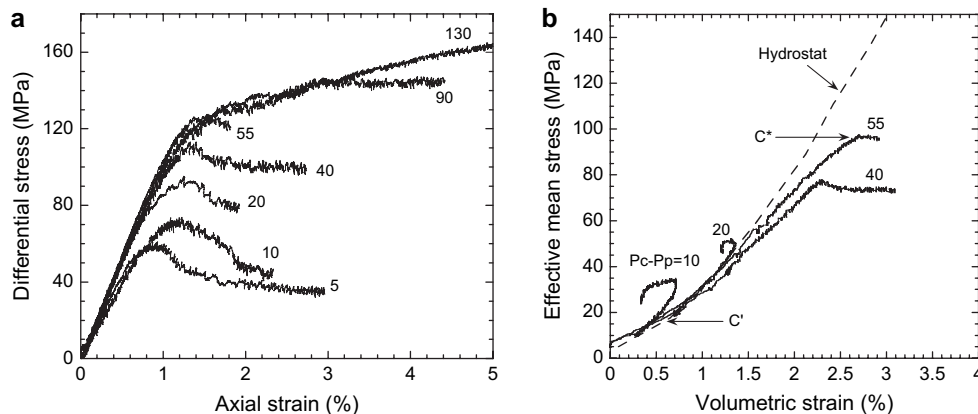


Fig. 2. (a) Differential stress versus axial strain for water saturated samples of Rothbach sandstone cored perpendicular to the bedding and deformed triaxially at effective pressures ranging from 5 MPa to 130 MPa. Data are from Bésuelle et al. (2003), except for the two experiments at 10 MPa and 130 MPa effective pressure which are from this study. (b) Effective mean stress versus volumetric strain in the Rothbach sandstone for four different values of effective pressure showing the transition from dilatant brittle faulting to shear-enhanced compaction. For reference, the hydrostat is shown as a dashed curve. The initial yield stresses C' for the onset of shear-induced dilation and C^* for the onset of shear-enhanced compaction are indicated by the arrows for the experiments at effective pressure 10 MPa and 55 MPa, respectively.

The effect of bedding on the brittle strength and compactive yield stress in sandstones was analyzed by Baud et al. (2005), who concluded that there is an overall trend for the strengths and yield stresses of samples cored perpendicular to the bedding to be higher than those parallel to the bedding. To investigate the influence of the bedding on the development of strain localization associated with compactive failure in Rothbach sandstone, the samples RotP3, RotQ3 and RotH4 were triaxially compressed at the same pressure conditions (140 MPa confining pressure and 10 MPa pore pressure) to axial strains of $\sim 3\%$. The differential stress and AE rate as functions of axial strain for these tests are presented in Fig. 3a–c. The effective mean stress as a function of porosity change is shown in Fig. 3d. The stress–strain curves for the three samples cored in three different directions are qualitatively similar in that they all show strain hardening and shear-enhanced compaction beyond the compactive yield strength C^* (marked in the figures). However, there seem to be subtle differences in the AE activity. While at least two upsurges in AE activity were observed for the other two samples, AE activity was almost constant in the sample RotH4 (cored parallel to bedding) when stressed to beyond C^* . In light of the conclusion of Baud et al. (2004) that such differences in AE activity may signify

differences in failure mode, the data suggest the possibility that these samples cored in different orientations may have failed by different modes of strain localization.

4. Digital correlation of radiographs

Digital radiographs acquired in the sample RotP3 before and after triaxial compression are shown in Fig. 4a (raw images) and Fig. 4b (after X-ray lighting correction and selection of the working window). Unlike in typical X-ray CT images, the data here were not processed and the gray level range represents the total amount of radiation that passed through the sample. Therefore, the more attenuating a zone, the darker it appears on the image (while the opposite is usually observed in X-ray CT images). The images for the undeformed and deformed states show almost identical patterns of heterogeneities, with subparallel arrays of relatively dense sedimentary layers. Since the spatial distribution of CT-value is dominated by bedding heterogeneity, the density changes associated with potential strain localization in the deformed sample cannot be readily resolved. In this study, we attempted to map out the strain pattern by comparing the images for the undeformed and deformed states using digital image correlation (DIC).

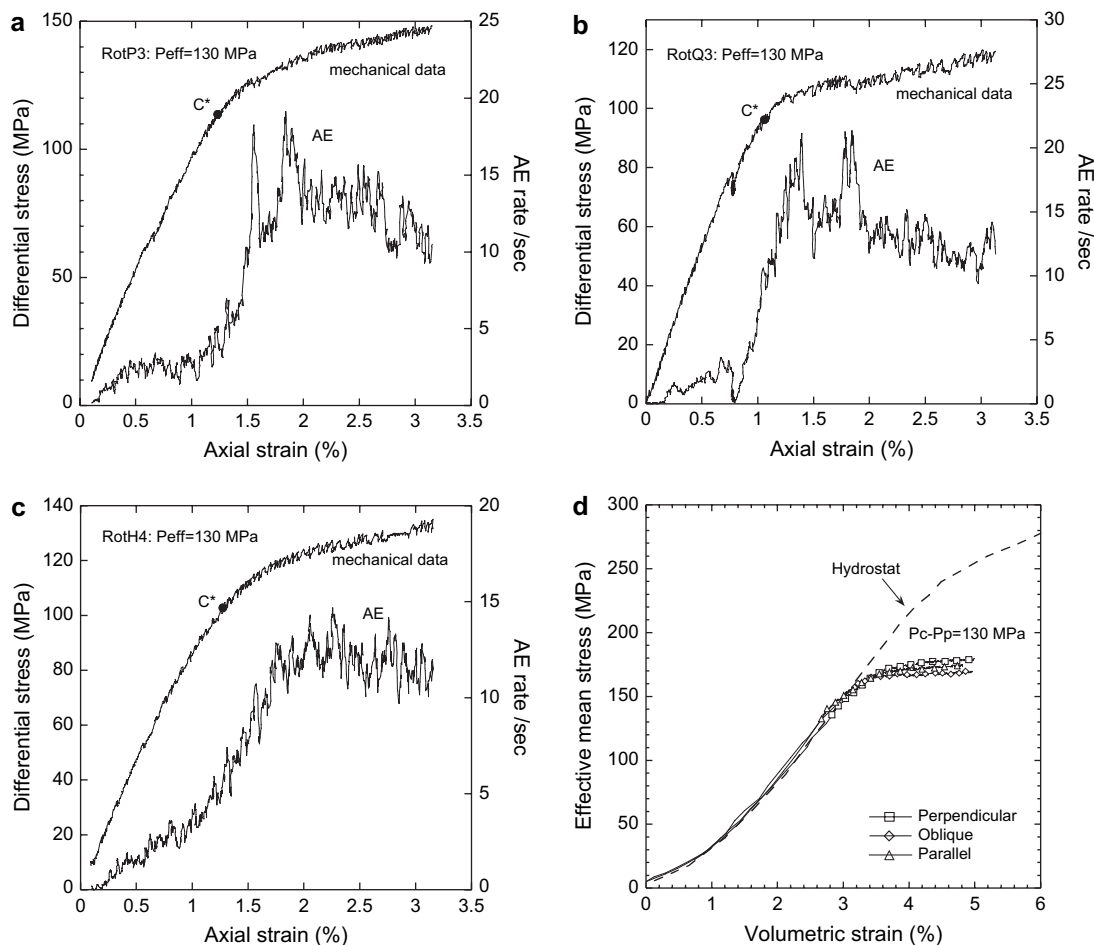


Fig. 3. (a)–(c) Differential stress and rate of acoustic emission as function of axial strain for three samples of Rothbach sandstone triaxially compressed at 130 MPa effective pressure. The samples were cored (a) perpendicular, (b) 45° and (c) parallel to the bedding. (d) Effective mean stress versus volumetric strain for the three samples. For reference, the hydrostat is shown as a dashed curve. The yield stresses C^* for the onset of shear-enhanced compaction are indicated.

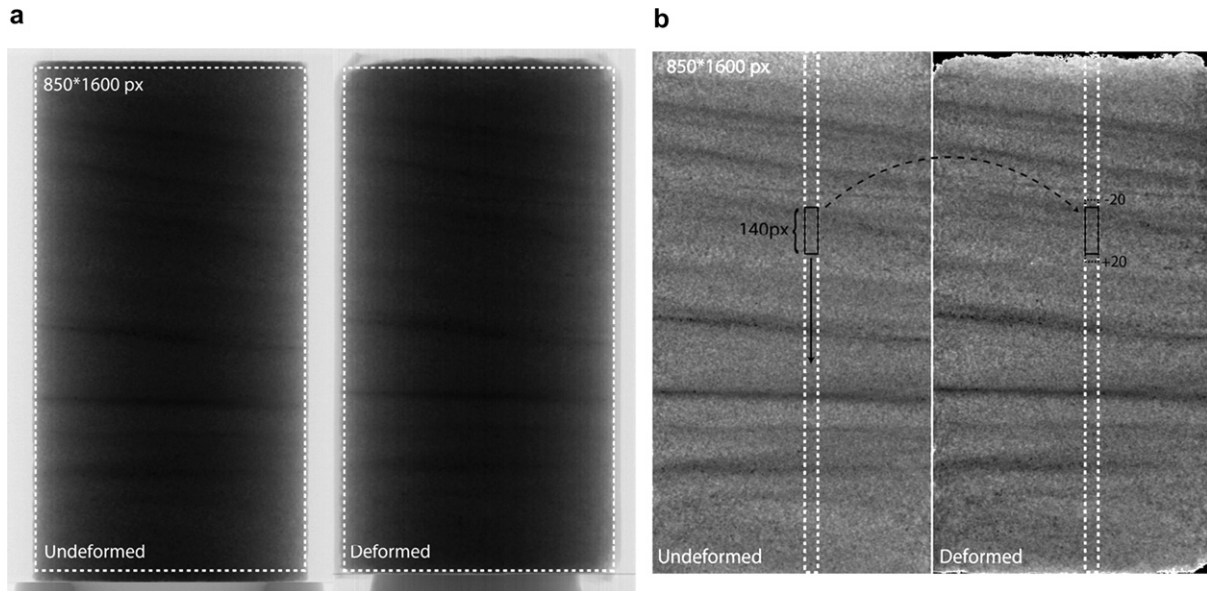


Fig. 4. (a) Digital radiographs of the Rothbach sample RotP3 (perpendicular to bedding) before and after triaxial compression. (b) The same images after correction from the transverse lighting fluctuation (due to change in thickness) and selection of the working window. The procedure followed for DIC consists in sampling short stripes in the image of the undeformed sample and determining its new vertical position in the image of the deformed sample.

DIC is used to infer an inelastic displacement field from two digital images of the same object acquired before and after a deformation increment has been applied. This technique has been applied extensively to characterize the deformation and failure in engineering materials. The basic principles of DIC and an overview of its applications were presented by Bruck et al. (1989) and Sutton et al. (2000), respectively. DIC was also used to probe the nucleation and development of damage in synthetic (Russell and Sutton, 1989; Bastawros et al., 2000; Wattrisse et al., 2001) and biomedical (Bay et al., 1999; Wang and Cuitiño, 2002) materials, and more recently in geomaterials (Rechenmacher and Finno, 2004; Bhandari and Inoue, 2005; Lenoir, 2006).

Consider a subset of neighboring pixels on the radiograph in the undeformed sample. With reference to the coordinate system shown in Fig. 1, the initial coordinates of an arbitrary point located within this subset of pixels are denoted by (y, z) , and the gray level that corresponds to its CT-value is denoted by $F(y, z)$. In the deformed sample the displaced coordinates and the corresponding gray level from CT-measurement will be denoted by (y^*, z^*) and $G(y^*, z^*)$, respectively. If the displacement field of the point located at the center of the selected subset of pixels is denoted by (v, w) , then the coordinates (y, z) of the arbitrary point in the undeformed state and the corresponding point (y^*, z^*) in the deformed state are related by:

$$y^* = y + v + \frac{\partial v}{\partial y} \Delta y + \frac{\partial v}{\partial z} \Delta z$$

$$z^* = z + w + \frac{\partial w}{\partial y} \Delta y + \frac{\partial w}{\partial z} \Delta z$$

where Δy and Δz denote distances from the subset center to the arbitrary point (y, z) . The partial derivatives are included

to account for the non-uniform strain field that exists in the subset. If the grain-scale heterogeneity in the undeformed sample (as manifested by the statistical variation of CT-values) was preserved in the deformed sample, then the correspondence between undeformed and deformed coordinates of the same material points in the sample can be identified by maximizing a normalized cross-correlation coefficient defined as follows:

$$C\left(y, z, v, w, \frac{\partial v}{\partial y}, \frac{\partial v}{\partial z}, \frac{\partial w}{\partial y}, \frac{\partial w}{\partial z}\right) = \frac{\sum[F(y, z)G(y^*, z^*)]}{\sqrt{\sum(F(y, z))^2 \sum(G(y^*, z^*))^2}}$$

The values of y, z, v and w that maximize the function C will provide the best estimates for the displacement and strain fields within the subset of pixels. While the displacement gradient terms have been demonstrated to improve the strain resolution in certain applications (Bruck et al., 1989), this was not formally incorporated into the correlation algorithm here because the quality of our data renders it very difficult to extract meaningful results from such a refined analysis. Indeed, since the pixel values are averaged over the entire thickness of the specimen, the small-scale texture of the image is not expected to hold after mechanical compaction and focus should be placed on the correlation values associated with larger scale heterogeneities such as laminations (size > 10 pixels). For a similar reason we were not able to extract data on the lateral displacement v due to its relatively small magnitude (as estimated in a later section). Hence in this preliminary study, DIC was used specifically to infer the axial displacement $w(y, z)$ by maximizing the cross-correlation function $C(y, z, w)$.

In our implementation, we considered a subset made up of 50 pixels in the lateral (y) direction and 140 pixels in the axial (z) direction, corresponding to a rectangular area of $\sim 1 \times 3 \text{ mm}^2$ (Fig. 4b). Each radiograph has 1600×850

pixels, from which an axial strip 50 pixels wide was first extracted. CT-values of the 50 pixels at the same axial location were averaged laterally to give column vectors F_i and G_i (with $i = 1, \dots, 1600$) for the undeformed and deformed states, respectively. From the column vector for the undeformed state, we then selected a subset made up of 140 consecutive elements, to form a column vector f_j (with $j = 1, \dots, 140$) such that $f_j = F_{i-1+j}$. Similarly a column vector g_j^o for the deformed state was defined such that $g_j^o = G_{i-1+j}$, and we then evaluated the cross-correlation coefficient C for the column vectors f_j and g_j^o . The coefficient was evaluated in 40 additional iterations; in each iteration the column vector for the deformed state was selected from elements shifted in the axial direction by n pixels, such that for the n th iteration it would be given by the vector $g_j^n = G_{i+n-1+j}$. Our iterations were performed within an axial range of ± 20 pixels, so that $n = -20, -19, \dots, 0, \dots, 19, 20$. The value of n that maximized the coefficient C was then multiplied by the pixel size to give a best estimate of the axial displacement w at the center of rectangular area made up of the 50×140 pixels.

We then considered the next subset of 140 consecutive elements in the undeformed state by shifting in the axial direction by 10 pixel lengths, which would revise the column vector to attain values $f_j = F_{i+9+j}$ (with $j = 1, \dots, 140$). The search for the best estimate of axial displacement would then be pursued in the same manner as discussed above. Repeating this process at axial increments of 10 pixels we derived estimates of the axial displacement w (averaged laterally over 50 pixel widths or 1.06 mm) at 142 locations with axial spacing of 10 pixel length or $\Delta z = 0.2$ mm.

Having completed this calculation for an axial strip, the procedure was repeated for adjacent stripes by shifting laterally over a distance equivalent to 10 pixels. Hence for a given axial location we would obtain 81 estimates of the axial displacement at lateral spacing of 10 pixel width or $\Delta y = 0.2$ mm. For each of the three samples we obtained a map of the axial displacement characterized by a 142×81 matrix at spacings of $\Delta y = \Delta z = 0.2$ mm. Estimations for the local strain components ε_{zz} and ε_{zy} were then obtained by calculating the gradient of the displacement values over vertical and horizontal samples of nine consecutive cells (~ 2 mm).

Before presenting our DIC it is important to address several limitations of our methodology. First, it is assumed that the only difference likely to be found between the two images arises from internal deformation within the sample, with negligible contribution to the relative displacement from slight changes in the positioning of the sample between the first and second radiographs. To match a set of images that were acquired at different times, in different conditions or with different sensors, various “image registration” techniques have been developed in computer vision for the identification of an optimal set of rigid body translations and rotations that would maximize the correlation among pairs of images. However, most of these techniques implicitly assume that the images in the set are identical, but in our case the images of the undeformed and deformed samples were not and therefore these registration techniques are not directly applicable. Fig. 5

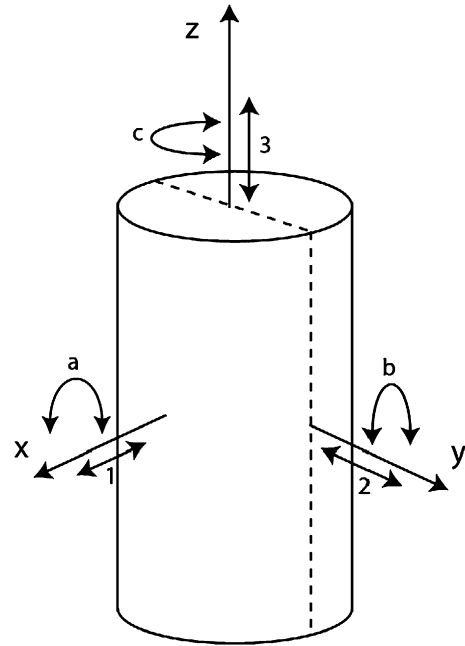


Fig. 5. Rock sample with the dashed line indicating the projection plane of the radiographs. Six potential transformations (three translations and three rotations) may occur due to slight misalignment of the sample during the acquisition of the second radiograph after the experiment.

shows a rock sample with a dashed line representing the marker we made on the exterior surface of the sample and the six potential transformations (translations (1)–(3) and rotations (a)–(c)) that could have occurred due to slight misalignment of the marker from the first to the second radiograph. Since we only considered data projected on the plane of the radiograph, translation (1) can be discarded. Translations (2) and (3) correspond to in-plane motions, which could perturb the absolute displacement by adding or subtracting a constant value along both axes. However, such constant displacements do not contribute to the strain field which depends only on relative displacements. Rotations (a) and (b) would be minimal if at least one of the end surfaces of the cylindrical sample remained flat after it had been compacted. Finally, rotation (c) may distort an oblique band in the image, but since special care was taken to accurately position the markers in both runs we expect this effect to be small.

Second, it is assumed that the irrecoverable deformation experienced by samples RotP3, RotQ3 and RotH4 was dominated by pure shortening in the axial direction, so that the transverse deformation can be neglected. The error so introduced can be estimated from our mechanical data if one assumes that potential thickening is distributed evenly along the sample tested. Using the Young’s modulus and bulk modulus inferred from elastic deformation, one can evaluate the elastic strains at a given stress state which can then be subtracted from the total strains to give the plastic strains. For the conventional triaxial configuration, Wong et al. (1997) defined the inelastic compaction factor $\Delta \varepsilon_v^p / \Delta \varepsilon^p$ to be the ratio between the plastic volumetric strain and plastic axial strain. Following their approach we inferred the inelastic compaction

factors in samples RotP3, RotQ3 and RotH4 to be 0.89, 0.85 and 0.83, respectively, on the basis of data from the onset of shear-enhanced compaction to 1% of plastic volumetric strain. In our calculations we used a bulk modulus value of 6.7 GPa (inferred from the slope of the hydrostat) and Young's modulus values of 11.7, 9.5 and 8.5 GPa (inferred from the initial slopes of the stress–strain curves in Fig. 3) for samples RotP3, RotQ3 and RotH4, respectively. Recently Baud et al. (in press) suggested the use of the plastic Poisson's ratio ν^p , defined in terms of the ratio between the plastic transverse and axial strains ($-\text{d}\varepsilon_3^p/\text{d}\varepsilon_1^p$) which is linearly related to the inelastic compaction factor by $\nu_p = (1 - \Delta\varepsilon_v^p/\Delta\varepsilon^p)/2$. The plastic Poisson's ratio is equal to 0.06, 0.08 and 0.09 for our three Rothbach sandstone samples cored in different orientations, which implies that the permanent axial strains (averaged over the sample length) are larger than the transverse strains (averaged over the sample diameter) by an order of magnitude. As will be shown in the next paragraph, an overall axial shortening of 8–14 pixels was observed depending on the sample. After accounting for the length-to-diameter ratio of about 2:1 a transverse expansion of <1 pixel would then be expected, a feature difficult to resolve by DIC unless we had used a significantly smaller pixel dimension.

Lastly, during the iteration process the displacement measurement routine may encounter difficulties in that poor coherence between profiles may produce noises with high spatial frequency manifested by anomalously high displacement gradients between neighboring windows (Bay et al., 1999). We filtered out such noises by allowing a maximum gradient value of 5 pixels along the 10 pixels separating these windows. Every discarded displacement value was replaced by the one in the preceding cell.

5. Strain localization and spatial distribution of damage

To describe the failure modes we will adopt the classification of deformation bands presented recently by Aydin et al. (2006). Deformation bands are structures that develop by the localization of strain into narrow tabular bands. A deformation band is classified kinematically as a “shear” or “volumetric” deformation band according to whether the localized deformation is predominantly by shearing or volume change. The localized deformation in a shear band may involve a certain

amount of volume increase or decrease, and accordingly these bands can be further distinguished to be either “compactive” or “dilatant” shear bands. If a volumetric deformation band was solely subjected to volume reduction or expansion, it is called a “compaction band” or “dilation band”. Based on their experimental observations (primarily on compaction bands), Baud et al. (2004) proposed to further refine the classification of deformation bands: a localized structure that has a thickness of only a few (say ≤ 3) grains is referred to as a “discrete band”, whereas thicker structures are called “diffuse band”.

After the X-ray radiographs had been acquired, the deformed samples were cut along the plane as indicated by the marker in Fig. 5 and petrographic thin sections were prepared. The spatial distribution of damage was quantified under an optical microscope. The thin section was divided into elemental squares 750 μm wide, and following Louis et al. (2005) and Menéndez et al. (1996) we defined a damage index in terms of the crack density (average number n of cracks per grain). The damage index has a value of I for an elemental square with $0 \leq n < 2$, II for $2 \leq n < 5$ cracks, III for $5 \leq n < 10$ cracks and IV for $n \geq 10$. Fig. 6 presents typical microstructures associated with these four levels of damage. It can be seen that the stress-induced damage was primarily due to grain crushing and pore collapse, as described by Bésuelle et al. (2003).

Fig. 7 shows the axial displacements (averaged over the diameter) in the three samples evaluated by DIC. To help visualize the general trends the data were smoothed and interpolated to derive the continuous profiles shown in color. There are fundamental differences among the average displacement profiles for the three samples. First, the axial shortening of sample RotQ3 was $\sim 50\%$ larger than those of the other two samples. This contrast can be attributed to differences in the Young's moduli of the samples tested but also to the unknown fraction of irrecoverable strain at the samples ends that could not be estimated due to the highly irregular and fragile nature of these zones. Second, while the profile for sample RotH4 shows an almost linear trend, the profiles for samples RotP3 and RotQ3 are characterized by several localized zones with anomalously large gradients in average axial displacement. In sample RotP3 at least four such zones can be discerned, and similarly two such zones can be identified

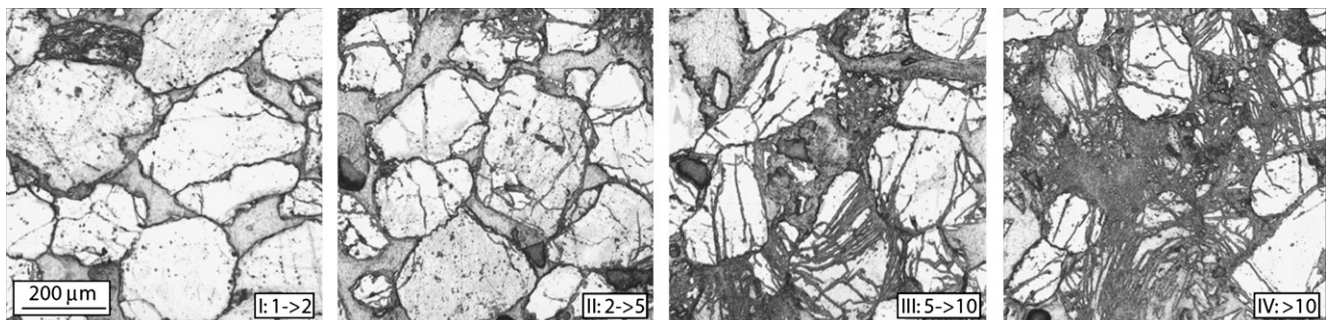


Fig. 6. Microstructure associated with the four levels of crack density (I–IV). The crack density range corresponding to each damage level is as indicated.

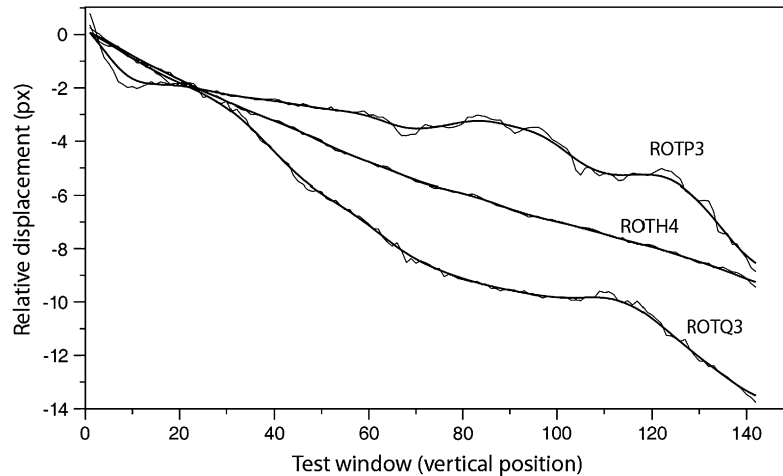


Fig. 7. Vertical displacement profiles averaged over the width for samples RotP3, RotQ3 and RotH4. Sample RotQ3 exhibits a relatively large overall shortening. While sample RotH4 shows an almost linear trend, samples RotP3 and RotQ3 show nonlinear fluctuations indicative of strain localization.

in sample RotQ3. To map out the spatial heterogeneity in strain corresponding to such nonlinear variations in displacement, the 142×81 matrix for each sample that characterizes the spatial distribution of axial displacement w at spacings of $\Delta y = \Delta z = 0.2$ mm was differentiated with respect to y and z to derive the displacement gradients $\partial w / \partial y$ and $\partial w / \partial z$.

Fig. 8a and b shows the spatial distribution of CT-values for sample RotP3 and the axial strain $\varepsilon_{zz} = \partial w / \partial z$ inferred from DIC, respectively. This sample was cored perpendicular to bedding, and at least five planar features with relatively high density can be identified from the distribution of CT-values.

The DIC indicates three localized zones with relatively high strains (up to 3×10^{-3}) which have extended across the sample subparallel to bedding. We marked with dashed white lines in these figures the area over which the damage index was characterized. The damage data were interpolated to give the damage map shown in Fig. 8c. Under the optical microscope we also delineated zones of relatively low porosity that correspond to bedding, and they are highlighted in white in Fig. 8d. Comparison of Fig. 8b and c establishes the spatial correspondence between strain localization features (inferred from DIC) and intense damage (inferred from microstructural

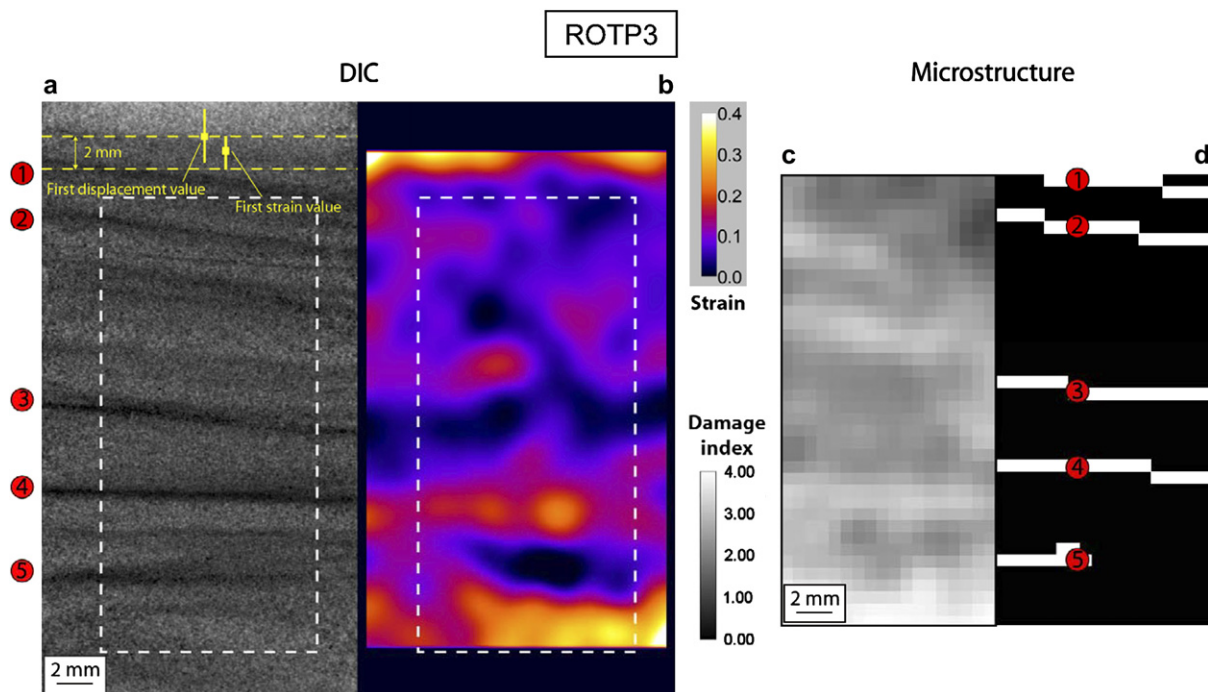


Fig. 8. Spatial distribution of the (a) X-ray attenuation values and (b) local axial strain in sample RotP3 cored perpendicular to the bedding. (c) Damage map obtained from thin section analysis. The white stripes in (d) are dense laminae identified from thin section. The white dotted line in (a) and (b) mark the area covered by the damage map (c).

observations). Since these features are subperpendicular to σ_1 with widths on the order of several grain diameters, we will classify them as “diffuse compaction bands”. In this sample these volumetric deformation bands typically developed in more porous regions that fall outside the five relatively dense zones associated with bedding, indicating that the development of compaction localization was inhibited inside the bedding laminations.

Fig. 9a and b shows the spatial distribution of CT-values for sample RotQ3 and the axial strain inferred from DIC, respectively. This sample was cored at 45° to bedding, and at least three planar features with relatively high density can be identified. The DIC indicates a high-strain zone subparallel to bedding that is located near the lower end of the sample. There is also a very diffuse high-strain zone that almost covers the upper half of the sample. Its geometry is suggestive of a diffuse deformation band parallel to the bedding that cuts across the sample, intersected by several shorter deformation bands along the conjugate direction. We marked with dashed white lines in these figures the area over which the damage index was characterized. Again comparison of Fig. 9b with the damage map in Fig. 9c establishes the spatial correspondence between strain localization and intense damage. Since these features are oriented at $\sim 45^\circ$ to σ_1 , we will classify them as “compactive shear bands”. In this sample the compactive shear bands seem to develop also in more porous regions that fall outside the three zones associated with bedding (Fig. 9a and d), thus indicating that the development of shear localization was inhibited in the bedding laminations.

The sample RotH4 was cored parallel to bedding, which is highlighted by the relatively thin zones of low density shown in Fig. 10a. In contrast to the other two samples, the strain map (Fig. 10b) does not reveal any continuous deformation bands with anomalously high strain cutting across this sample. This is not surprising in light of the almost linear trend of displacement shown in Fig. 7. The absence of strain localization is manifested by a spatial distribution of damage that seems homogeneous (Fig. 10c). Overall the magnitudes of permanent strain and damage in this sample are lower than those in the other two samples.

If the lateral displacement v and its gradient $\partial v/\partial z$ can be neglected, then the shear strain can be approximated by $\varepsilon_{zy} = (1/2)(\partial w/\partial y)$. From the mechanical data we inferred that the displacement component v was smaller than the axial displacement w by an order of magnitude. Unless v fluctuates over axial distances that are shorter than the wavelengths of the strain localization (Figs. 8b and 9b) by as much as an order of magnitude, we would expect the gradient $\partial v/\partial z$ to be so small that it can be neglected. Using this approximation we calculated the strain components ε_{zz} and ε_{zy} from the axial displacement field inferred by DIC. Assuming a two-dimensional strain field (with $\varepsilon_{yy} \approx 0$) we can then use Mohr circle analysis to evaluate the principal strains and their orientations (Fig. 11). The principal strains will be denoted by ε_M and ε_m , with $\varepsilon_M \geq \varepsilon_m$.

The principal strain ε_M in all three samples was inferred to be compressive with magnitude comparable to the axial strain ε_{zz} . In contrast the principal strain ε_m had relatively small magnitude, and it was actually extensile in many locations. In the

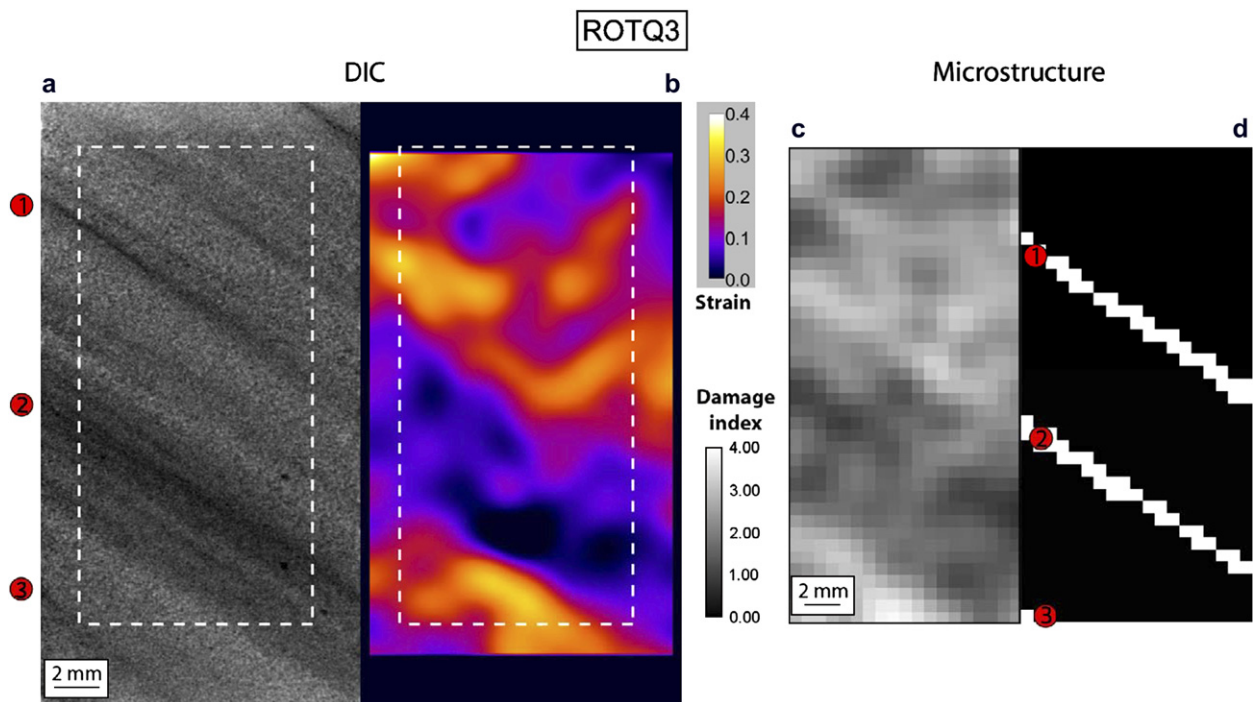


Fig. 9. Spatial distribution of the (a) X-ray attenuation values and (b) local axial strain in sample RotQ3 cored at angle 45° to the bedding. (c) Damage map obtained from thin section analysis. The white stripes in (d) are dense laminae identified from thin section. The white dotted line in (a) and (b) marks the area covered by the damage map (c).

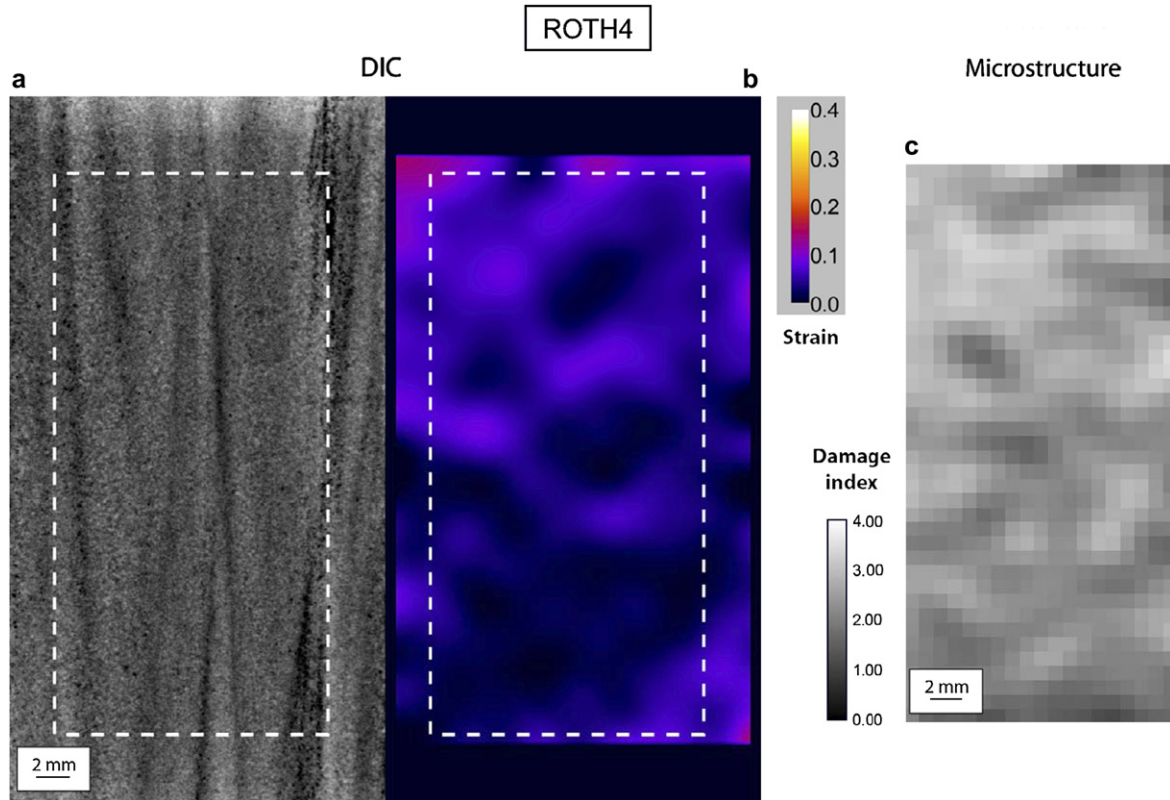


Fig. 10. Spatial distribution of the (a) X-ray attenuation values and (b) local axial strain in sample RotH4 cored parallel to the bedding. (c) Damage map obtained from thin section analysis.

two samples RotP3 and RotQ3 locations with relative high values of ε_M (Fig. 11a and b) are usually associated with relatively high values of ε_{zz} (Figs. 8b and 9b) and orientation of this principal strain were predominantly subparallel to σ_1 . In sample RotH4 magnitudes of the principal strains were small. The strain distribution was relatively homogeneous and orientation of the principal strain ε_M was deviated appreciably from the σ_1 direction.

6. Discussion

In typical DIC applications, the images are acquired in situ while the sample is being deformed. In a triaxial compression configuration this is not very practical unless pressure vessels with optically transparent windows are specially designed for this purpose. It was therefore necessary in our study to deform the jacketed sample inside the pressure vessel and then retrieve it after the experiment so that the radiograph of the failed sample can be acquired. Even though special care was undertaken to ensure the accurate positioning of the exterior marker (Fig. 5), there were many uncertainties which might introduce ambiguities into the interpretation of the strain distribution inferred by DIC. Nevertheless, our preliminary results demonstrate the feasibility of this approach for mapping out strain localization in triaxially compressed rock samples. Although the thin sections analyzed are representative of a plane only (what may explain some of the apparent discrepancies with

the strain maps in Figs. 8 and 9), quantitative characterization of the spatial distribution of damage provides validation of our strain data. Since the microstructural observations were tedious and time-consuming, the methodology developed here using DIC of CT image provides an efficient and effective alternative.

This feasibility study suggests several directions for future research. The acquisition of X-ray CT data with smaller voxel sizes would allow more comprehensive mapping of the 3D strain field at higher resolutions. As emphasized before an advantage of DIC is that it is not restricted to samples that are homogeneous or isotropic, and therefore the technique is particularly appropriate for applications related to a material as complex as a rock. In this study an “industrial” CT was used for the imaging, but it should be noted that significantly more refined resolution is available using synchrotron CT (e.g. Fredrich et al., 2006).

We have focused on the compactive failure in a porous sandstone associated with strong bedding anisotropy. Three samples were cored in different orientations relative to bedding, and by imaging the samples that failed under identical pressure conditions and at comparable strain our data underscore the significant control of bedding over the failure mode. The samples show three fundamentally different patterns of strain localization. While diffuse compaction bands developed in the sample RotP3 cored perpendicular to bedding, compactive shear bands were observed in RotQ3 cored

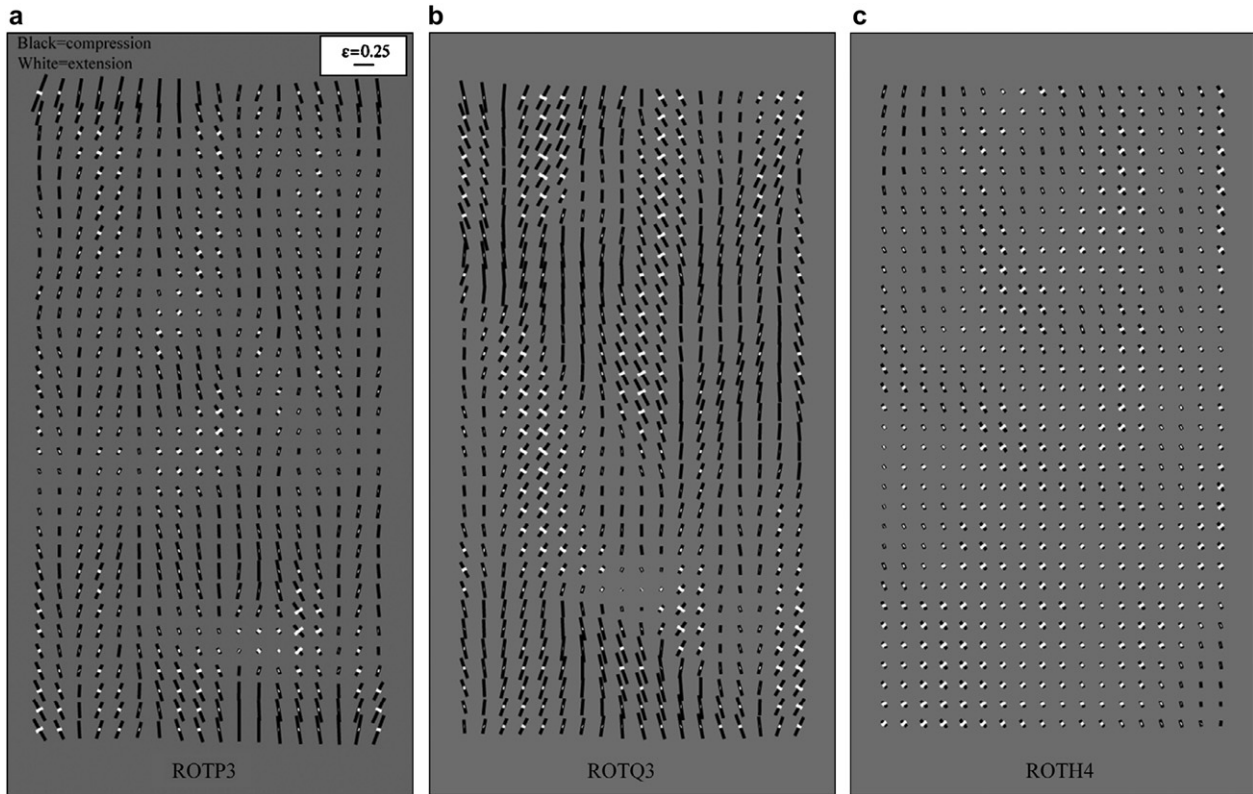


Fig. 11. Direction and magnitude of local principal strains obtained by diagonalization using calculated values of ε_{zz} and ε_{zy} and assuming ε_{yy} to be zero in samples RotP3 (a), RotQ3 (b) and RotH4 (c).

at 45° to bedding. Hence the bedding seems to have guided the development of the diffuse deformation bands. It has also apparently controlled the location of strain localization since the compactive failure developed primarily in regions outside the relatively dense laminations. In the sample RotH4 cored parallel to bedding, the strain and damage were smaller and relatively distributed. It is plausible that the laminations acted as the stress-supporting framework, thus alleviating strain localization in the more porous zones.

We have considered samples deformed under only one effective pressure condition. To gain a deeper understanding of the influence of bedding anisotropy on the mechanics of strain localization and micromechanics of failure, it is desirable to extend the investigation to a wider range of pressure conditions. Such a systematic study is currently conducted in our laboratory and we intend to present the related results in a future publication.

Acknowledgments

We thank Jean Schmittbuhl and Brent Lindquist for stimulating discussions. The X-ray scanning was conducted by Richard Ketcham at the High-Resolution X-ray Computed Tomography facility at the University of Texas at Austin, an NSF-supported multi-user facility (grant EAR 0345710) and we thank him for acquiring these high quality data. During the image processing, extensive use of Scilab (freeware INRIA) and ImageJ (freeware NIH) was made. We are grateful

to Pierre Bésuelle and Richard Ketcham for their thorough reviews. The research at Stony Brook was partially supported by the National Science Foundation under grant EAR-0310087 and by the Department of Energy under grant DE-FG02-99ER14996.

References

- Arns, C.H., Knackstedt, M.A., Val pinczewski, W., 2001. Accurate estimation of transport properties from microtomographic images. *Geophysics Research Letters* 28 (17), 3361–3364.
- Arns, C.H., Knackstedt, M.A., Val pinczewski, W., 2002. Computation of linear elastic properties from microtomographic images: methodology and agreement between theory and experiment. *Geophysics* 67 (5), 1396–1405.
- Aydin, A., Borja, R.I., Eichhubl, P., 2006. Geological and mathematical framework for failure modes in granular rock. *Journal of Structural Geology* 28 (1), 83–98.
- Bastawros, A.F., Bart-Smith, H., Evans, A.G., 2000. Experimental analysis of deformation mechanisms in a closed-cell aluminum alloy foam. *Journal of the Mechanics and Physics of Solids* 48 (2), 301–322.
- Baud, P., Klein, E., Wong, T.-f., 2004. Compaction localization in porous sandstones: spatial evolution of damage and acoustic emission activity. *Journal of Structural Geology* 26, 603–624.
- Baud, P., Louis, L., David, C., Rawling, G.C., Wong, T.-f., 2005. Effects of bedding and foliation on mechanical anisotropy, damage evolution and failure mode. In: Bruhn, D., Burlini, L. (Eds.), *High-strain Zones: Structure and Physical Properties*. Geological Society of London, Special Publication, vol. 245, pp. 223–249.
- Baud, P., Vajdova, V., Wong, T.-f. Shear-enhanced compaction and strain localization: inelastic deformation and constitutive modeling of four porous sandstones. *Journal of Geophysical Research*, in press.

- Bay, B.K., Smith, T.S., Fyhrie, D.P., Saad, M., 1999. Digital volume correlation: three-dimensional strain mapping using X-ray tomography. *Experimental Mechanics* 39 (3), 217–226.
- Bésuelle, P., Baud, P., Wong, T.-f., 2003. Failure mode and spatial distribution of damage in Rothbach sandstone in the brittle–ductile transition. *Pure and Applied Geophysics* 160, 851–868.
- Bhandari, A.R., Inoue, J., 2005. Strain localization in soft rock – a typical rate-dependent solid: experimental and numerical studies. *International Journal for Numerical and Analytical Methods in Geomechanics* 29 (11), 1087–1107.
- Bruck, H.A., McNeill, S.R., Sutton, M.A., Peters, W.H., 1989. Digital image correlation using the Newton–Raphson method of partial-differential correction. *Experimental Mechanics* 29 (3), 261–267.
- Chu, T.C., Ranson, W.F., Sutton, M.A., Peters, W.H., 1985. Applications of digital-image-correlation techniques to experimental mechanics. *Experimental Mechanics* 25 (3), 232–244.
- Desrues, J., Chambon, R., Mokni, M., Mazerolle, F., 1996. Void ratio evolution inside shear bands in triaxial sand specimens studied by computed tomography. *Geotechnique* 46 (3), 529–546.
- Fredrich, J.T., Digiiovanni, A.A., Noble, D.R., 2006. Predicting macroscopic transport properties using microscopic image data. *Journal of Geophysical Research* 111, B03201, doi:10.1029/2005JB003774.
- Kawakata, H., Cho, A., Kiyama, T., Yanagidani, T., Kusunose, K., Shimada, M., 1999. Three-dimensional observations of faulting process in Westerly granite under uniaxial and triaxial conditions by X-ray CT scan. *Tectonophysics* 313, 293–305.
- Ketcham, R.A., 2005. Three-dimensional grain fabric measurements using high-resolution X-ray computed tomography. *Journal of Structural Geology* 27 (7), 1217–1228.
- Ketcham, R.A., Carlson, W.D., 2001. Acquisition, optimization and interpretation of X-ray computed tomographic imagery: applications to the geosciences. *Computers & Geosciences* 27, 381–400.
- Ketcham, R.A., Iturrino, G.J., 2005. Nondestructive high-resolution visualization and measurement of anisotropic effective porosity in complex lithologies using high-resolution X-ray computed tomography. *Journal of Hydrology* 302, 92–106.
- Lenoir, N., 2006. Comportement mécanique et rupture dans les roches argileuses étudiés par microtomographie à rayons X. PhD thesis, Université Joseph Fourier – Grenoble 1.
- Lindquist, W.B., Venkatarangan, A., Dunsmuir, J., Wong, T.-f., 2000. Pore and throat size distributions measured from synchrotron X-ray tomographic images of Fontainebleau sandstones. *Journal of Geophysical Research* 105, 21509–21527.
- Louis, L., Wong, T.-f., Baud, P., Tembe, S., 2005. Imaging strain localization by X-ray computed tomography: discrete compaction bands in Diemelstadt sandstone. *Journal of Structural Geology* 28 (5), 762–775.
- Menéndez, B., Zhu, W., Wong, T.-f., 1996. Micromechanics of brittle faulting and cataclastic flow in Berea sandstone. *Journal of Structural Geology* 18, 1–16.
- Paterson, M.S., Wong, T.-f., 2005. *Experimental Rock Deformation – The Brittle Field*, second ed. Springer-Verlag, New York.
- Raynaud, S., Fabre, D., Mazerolle, F., Geraud, Y., Latiere, H.J., 1989. Analysis of the internal structure of rocks and characterization of mechanical deformation by a non-destructive method: X-ray tomodensitometry. *Tectonophysics* 159, 149–159.
- Rechenmacher, A.L., Finno, R.J., 2004. Digital image correlation to evaluate shear banding in dilatative sands. *Geotechnical Testing Journal* 27 (1), 13–22.
- Renard, F., Bernard, D., Thibault, X., Boller, E., 2004. Synchrotron 3D microtomography of halite aggregates during experimental pressure solution creep and evolution of the permeability. *Geophysical Research Letters* 31, L07607.
- Russell, S.S., Sutton, M.A., 1989. Strain-field analysis acquired through correlation of X-ray radiographs of a fiber-reinforced composite laminate. *Experimental Mechanics* 29 (2), 237–240.
- Sutton, M.A., McNeill, S.R., Helm, J.D., Chao, Y.J., 2000. Advances in two-dimensional and three-dimensional computer vision. *Photo-Mechanics Topics in Applied Physics* 77, 323–372.
- Viggiani, G., Lenoir, N., Bésuelle, P., Di Michiel, M., Marelli, S., Desrues, J., Kretschmer, M., 2004. X-ray microtomography for studying localized deformation in fine-grained geomaterials under triaxial compression. *Comptes-rendus de Mécanique* 332, 819–826.
- Vinegar, H.J., De Waal, J.A., Wellington, S.L., 1991. CT studies of brittle failure in castlegate sandstone. *International Journal of Rock Mechanics and Mining Sciences* 28 (5), 441–448.
- Wang, Y., Cuitiño, A.M., 2002. Full-field measurements of heterogeneous deformation patterns on polymeric foams using digital image correlation. *International Journal of Solids and Structures* 39 (13–14), 3777–3796.
- Wattrisse, B., Chrysochoos, A., Muracciole, J.M., Nemoz-Gaillard, M., 2001. Analysis of strain localization during tensile tests by digital image correlation. *Experimental Mechanics* 41 (1), 29–39.
- Wellington, S.L., Vinegar, H.J., 1987. X-ray computerized tomography. *Journal of Petroleum Technology* 39, 885–898.
- Wong, T.-f., David, C., Zhu, W., 1997. The transition from brittle faulting to cataclastic flow in porous sandstones: mechanical deformation. *Journal of Geophysical Research* 102, 3009–3025.